minerals

MDPI

Article

Geochemical and Spectroscopic Features of Beryl (Aquamarine) from Renli No. 5 Pegmatite in Hunan, Central China

Ying Jiang [1], Jiankang Li [2], Peng Li [2,*], Yitao Cai [1] and Liping Zhang [3]

[1] School of Material Engineering, Jinling Institute of Technology, Nanjing 211169, China
[2] Key laboratory of Metallogeny and Mineral Resource Assessment, Institute of Mineral Resources, Chinese Academy of Geological Sciences, Beijing 100037, China
[3] 311 Brigade of Hunan Nuclear Geology, Changsha 410100, China
* Correspondence: lipeng031111@163.com

Abstract: The No. 5 pegmatite vein is the most evolved and well mineralized vein in the Renli deposit, with beryl being the most important beryllium mineral. The vein represents one of the most important gem-quality aquamarine mines at Renli. In this study, beryl crystals from the No. 5 pegmatite vein were examined by EMPA (electron microprobe analysis), ICP-MS (inductively coupled plasma-mass spectrometry), XRD (diffraction of X-rays), FTIR (fourier transform infrared spectrometer), and Raman analyses. Field and petrographic observations showed that most beryl crystals are euhedral to subhedral with light to medium blue color. EMPA analyses indicated that the main chemical compositions of beryl are close to the ideal values, with relatively low Fe (0.222–0.690 wt%) and alkali metal (0.280–0.820 wt%) contents. Geochemical and spectroscopic analyses indicated that cations replacement in beryl is relatively simple. The substituting cations of beryl in the octahedral Al site include mainly: Mg^{2+}, Fe^{2+}, Fe^{3+}, Mn^{2+}, Cr^{3+}, Ti^{4+}, and the excess Si. The tetrahedral Be site is mainly replaced by Li. Alkali metals in channel (esp. Na) serve as a charge compensator. According to the Fe-Mg-alkali and Li-Cs contents, the beryls from No. 5 pegmatite belong to the low Li-Cs and low Fe-Mg-medium alkali beryl groups. Field and geochemical data indicated that the No. 5 pegmatite vein formed by the multistage Mufushan granitic pluton emplacement and the magma source was less evolved.

Keywords: beryl; Renli pegmatite deposit; No. 5 pegmatite vein; chemical composition; spectroscopic characteristics; metallogenic mechanism; gemological significance

check for updates

Citation: Jiang, Y.; Li, J.; Li, P.; Cai, Y.; Zhang, L. Geochemical and Spectroscopic Features of Beryl (Aquamarine) from Renli No. 5 Pegmatite in Hunan, Central China. *Minerals* **2023**, *13*, 336. https://doi.org/10.3390/min13030336

Academic Editor: Nikita V. Chukanov

Received: 28 December 2022
Revised: 13 February 2023
Accepted: 24 February 2023
Published: 27 February 2023

1. Introduction

Rare metals, including Li, Be, Ni, Ta, Cs, Zr, Hf, and Rb, are strategic materials for various industries including aviation, aerospace, and green energy [1]. Beryl is both a Be ore mineral and a precious gemstone [2]. It is most abundant in granitic pegmatites, and occurs in highly evolved granites, hydrothermal veins, and occasionally in meta-mafic rocks [3–5]. As an accessory mineral, beryl can be formed at any stage of granitic pegmatite formation, and can thus coexist with minerals that crystallized across the magma fractionation sequence [4,5].

Pure beryl is colorless, and can have different colors (e.g., yellowish-green, green, blue, gray white, and light rose) due to the substitution of metal ions, including Cr^{3+}, V^{5+}, Fe^{2+}, Fe^{3+}, Mn^{2+}, Rb^{+}, and Cs^{+}. Among the various colors, the most famous ones are emerald green (due to Cr and V cations) and aquamarine blue (due to Fe cation) [1,6]. Both long- and short-prismatic beryl crystals are most common, but tabular crystals are also not rare [5,7]. As Cs and Li enter the crystal lattice, beryl changes from hexagonal to orthorhombic [5,7].

The composition and structure of beryl from different origins have been extensively studied [4,8–12]. Beryl is a cyclic silicate (structure very similar to cordierite [13]) with the ideal chemical formula of $Be_3Al_2Si_6O_{18}$. The stacked hexagonal rings of $(SiO_4)^{4-}$ tetrahedra are arranged along the crystallographic c-axis, forming a large open channel. Rings

of SiO_4 tetrahedra are connected with the Al octahedral and Be tetrahedral sites, forming a 3D framework. Many cations can be incorporated into the beryl structure, and these substitutions cause lattice distortion and changes in the bond-length and bond-angles [9,11,12,14–16]. These very complex crystal-chemical behaviors give beryl varying physical properties, such as specific gravity (SG) and refractive index (RI) [9,17]. The chemical composition and internal zoning characteristics of beryl can indicate the fractionation degree of pegmatitic magma, and the trace element compositional change (e.g., Na, Cs, Mg, and Fe) has important geochemical tracing significance [5,6,18,19].

The Renli deposit is a recently-discovered, super-large high-grade polymetallic granitic pegmatite deposit in China [20]. The No. 5 rare metal pegmatite vein is rich in Ta, Nb, Li, Be, Cs, and is the largest vein at Renli deposit [21]. At present, research on this vein had focused mainly on the pegmatite petrographic and geochemical features, whilst research on the beryl in pegmatite is very limited [21–23]. Here, we reported the geological characteristics of No. 5 pegmatite vein, as well as the geochemical and spectroscopic features of the beryl (aquamarine) therein, with the aim of establishing its formation mechanism and gemological significance.

2. Geological Background

2.1. Regional Geological Background

The Mufushan batholith is a composite granitoid, showing widespread rare-metal mineralization (Figure 1) [24,25]. Geographically, the Renli deposit is located in the southwestern exocontact of the Mufushan granite complex with the Lengjiaxi Group (in Pingjiang County, Hunan Province) [22] (Figure 1b). Tectonically, this deposit is located in the middle Jiangnan fold belt, which represents the Yangtze-Cathaysia suture zone [26] (Figure 1a). NE-trending faults are the main local structures, followed by NNW-trending ones (Figure 1b). The outcropping strata consist mainly of the Neoproterozoic Lengjiaxi Group and Quaternary sequences. The Lengjiaxi Group constitutes the metamorphic fold basement of the Yangtze block, and comprises a set of low-grade metamorphic clastic rocks (slate) with maximum thickness of 2.5 km [25,27]. The rock strata trend NW and dip SW, with a dip angle of 20–50° [25]. Magmatism was extensive in this area. Outcropping magmatic rocks include Neoproterozoic and Yanshanian (Jurassic-Cretaceous) granitoids: (i) Neoproterozoic medium-fine biotite plagioclase granite in the southeast; and (ii) Yanshanian Mufushan batholith in the north, which mainly comprises medium-fine two-mica monzogranite, fine-grained granodiorite, and medium-grained gneissic/porphyritic biotite monzogranite (Figure 1b) [24].

The ore-bearing granitic pegmatite veins are densely distributed in groups around the Mufushan composite batholith (Figure 1b). At present, 926 major outcropping pegmatite veins have been documented, among which 712 are from the granite intrusions and 214 are from the Lengjiaxi Group schist [22,24,25]. Local rare-metal pegmatites show regular lithological zoning and rare-metal mineral assemblages from the northeast to southwest (Figure 1b) [24]. The vein sizes decrease away from the batholith, and the rare-metal assemblage becomes increasingly complex (Be → Be + Nb + Ta → Be + Nb + Ta + Li) [24–27]. This zoning in pegmatite indicates a close genetic link between the Mufushan granite and rare-metal pegmatites [24].

2.2. Geology of the No. 5 Pegmatite Vein

The Renli No. 5 pegmatite vein is located in the Lengjiaxi Group schist (Figures 2 and 3a), 1.0–2.5 km away from Mufushan granite complex (Figure 1b) [20]. The vein is 4040 m long, with the maximum thickness of 10.1 m. This vein strikes NW, and dips toward the SE with a dip angle of 25–56° [23]. Field investigation combined with previous studies [21,22] showed that mineral and textural zoning is well developed in the No. 5 pegmatite vein. The zonation sequence is as follows (from the margin to the core): The graphic-textured zone I → coarse-grain microcline-albite zone II → medium-grained muscovite-albite zone III → fine-grained garnet-muscovite-albite zone IV → lepidolite-quartz core zone V [22]

(Figure 2). Zone I is characterized by typical quartz + microcline + albite graphic texture, with a grain size of 3–10 mm and band width of ~0.8 m (Figure 3b). Zone II, with a grain size of 7–15 mm and band width of ~4.7 m, is gradually transitioned from zone I (Figure 3b). The pegmatite consists of dominantly coarse-grained microcline and albite, associated with muscovite, quartz, beryl, and tantalite (Figure 3c). There is a gradual transition from zone II to III, as well (Figure 3d). Zone III, with a grain size of 5–10 mm and a band width of ~5.7 m, is composed mainly of medium-grained albite, microcline, quartz, and muscovite, along with minor euhedral blue-green aquamarine (Figure 3e). Zone IV, with a grain size of 1–5 mm and band width of ~5.7 m, has a sharp boundary with zone III (Figure 3f). It is composed mainly of fine-grained albite, quartz, garnet, microcline, and muscovite, along with minor short columnar aquamarine and fine-grained scaly lepidolite (Figure 3g–i). The lepidolite-quartz zone V (Figure 3j) has a grain size of 3–20 mm and band width of over 0.7 m. The main mineral assemblage includes lepidolite, quartz, albite, microcline, and elbaite (Figure 3k–l), as well as minor morganite, Cs-garnet, manganocolumbite, and columnar aquamarine (Figure 3l–o).

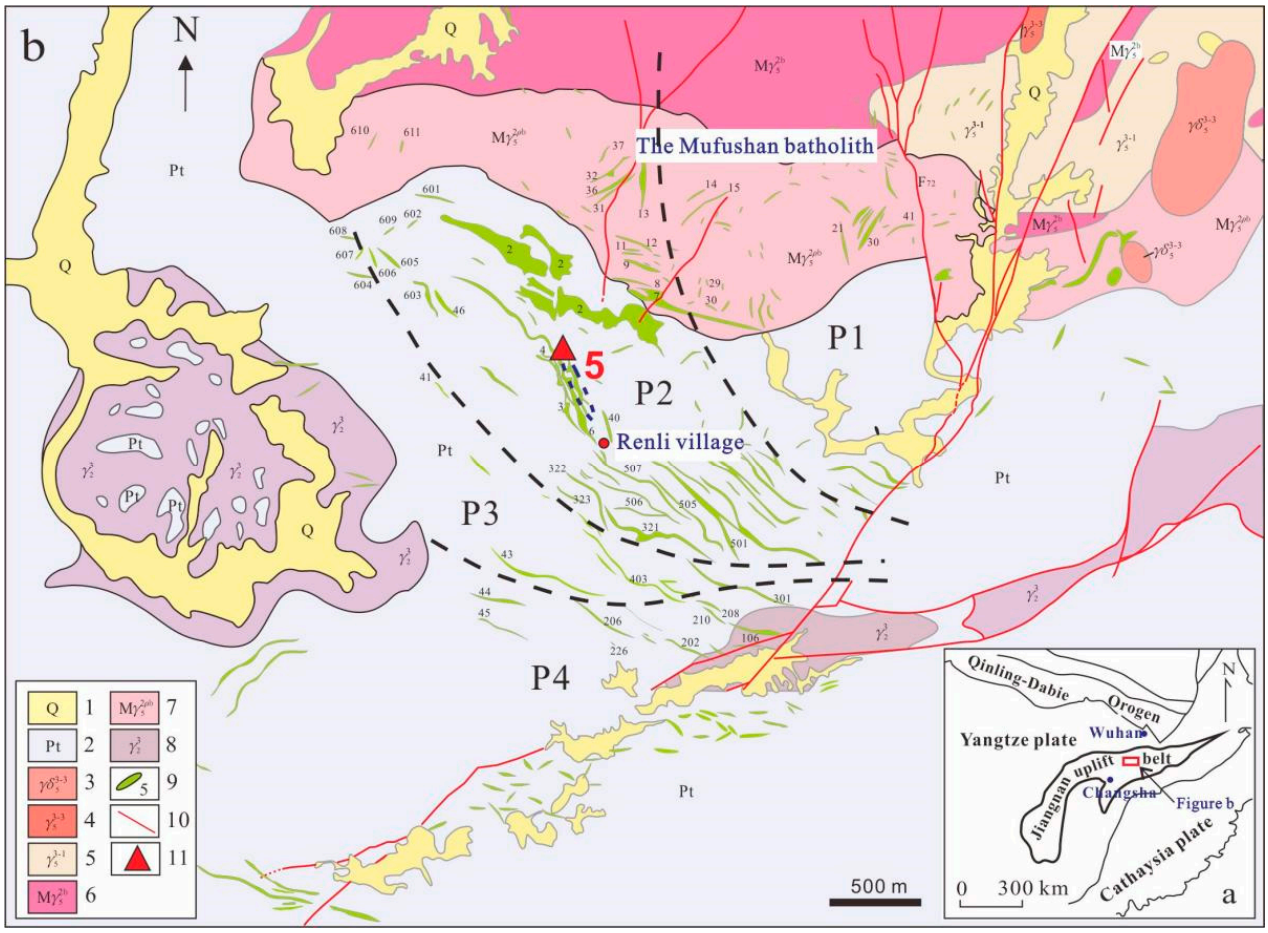

Figure 1. Simplified tectonic map (**a**) and geological map (**b**) of the Renli deposit (modified after [22]). 1—Quaternary alluvium; 2—Lengjiaxi Group; 3—fine-grained granodiorite; 4—fine-grained two-mica monzogranite; 5—medium-grained two-mica monzogranite; 6—medium-grained porphyritic biotite monzogranite; 7—medium-grained gneissic biotite monzogranite; 8—Neoproterozoic two-mica plagioclase granite; 9—pegmatite vein; 10—major faults; 11—sampling location. Pegmatite zones: P1—microcline type; P2—microcline-albite type; P3—albite type; P4—albite-spodumene type.

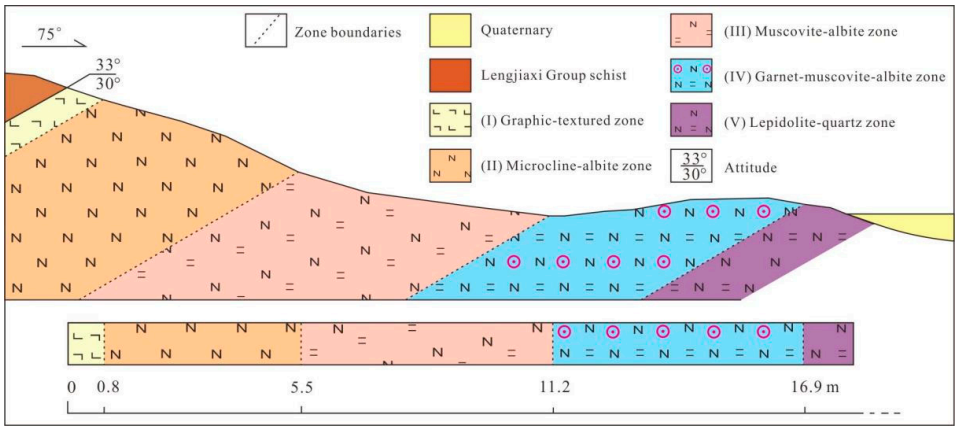

Figure 2. Geological profile of the Renli No. 5 pegmatite (modified after [22]).

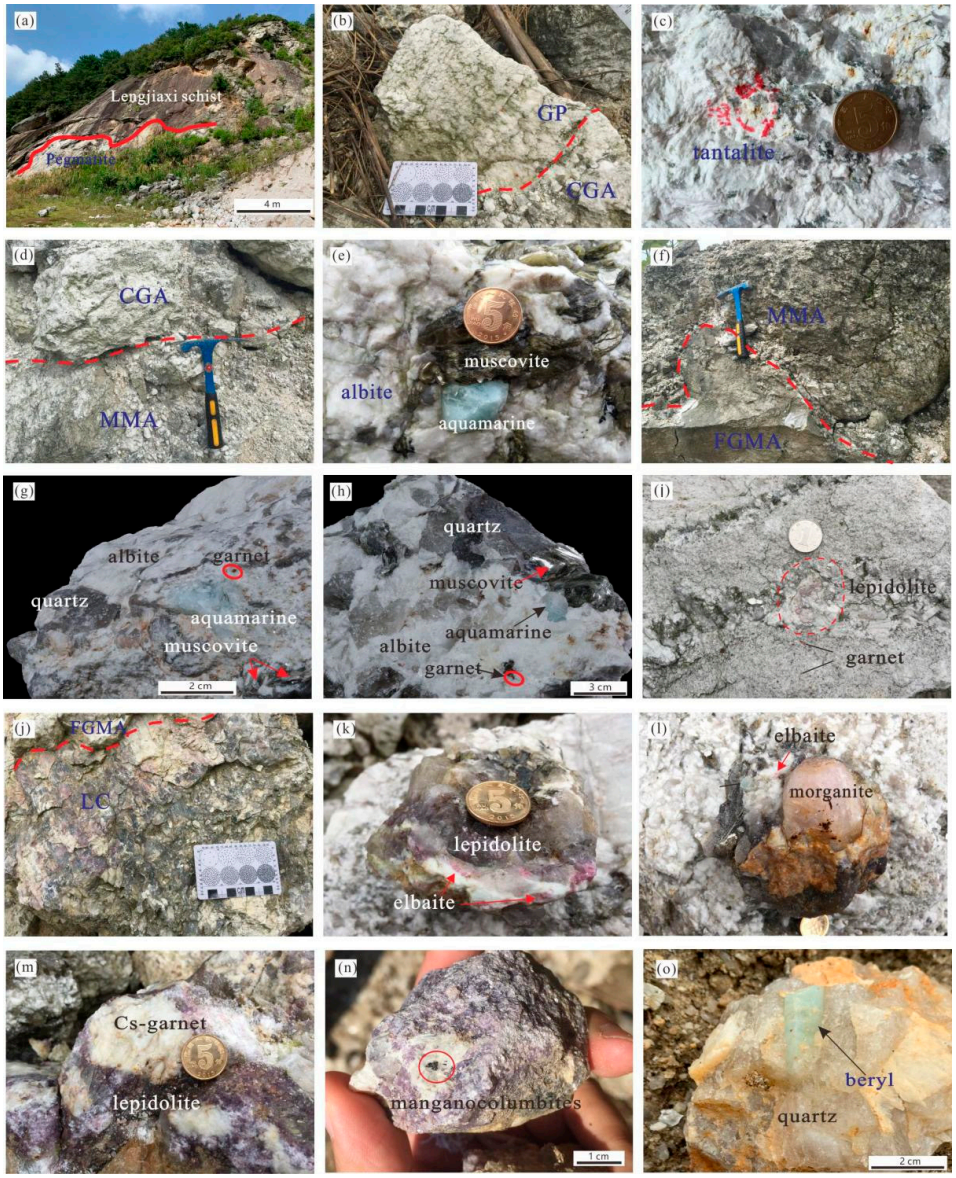

Figure 3. Field and sample photographs of the Renli No. 5 pegmatite. GP—graphic pegmatite, CGA—coarse-grained microcline-albite zone, MMA—medium-grained muscovite-albite zone, FGMA—fine-grained garnet-muscovite-albite zone, LC—lepidolite quartz core. (**a**) Contact relationship between

the Renli No. 5 pegmatite and Lengjiaxi Group schist; (**b**) contact between the graphic pegmatite and microcline-albite zones; (**c**) thin tabular columbite-tantalites are distributed mostly in massive albite; (**d**) contact between the microcline-albite and muscovite-albite zones; (**e**) short columnar aquamarine in the microcline-albite zone; (**f**) contact between the muscovite-albite- and garnet-muscovite-albite zones; (**g**,**h**) beryl in the garnet-muscovite-albite zone; (**i**) fine-grained scaly lepidolite and long columnar elbaite in the lepidolite-quartz core; (**j**) contact between the garnet-muscovite-albite and lepidolite-quartz core; (**k**) fine-grained scaly lepidolite and long columnar elbaite in the lepidolite quartz core; (**l**) morganite in the lepidolite-quartz core; (**m**) Cs-garnet in the lepidolite-quartz core; (**n**) manganocolumbite in the lepidolite-quartz core is distributed mostly in feldspars; (**o**) hexagonal aquamarine in the lepidolite-quartz core. (**b**–**f** and **i**–**n** are modified after [22]).

3. Materials and Methods

A total of 12 beryl samples were collected from the quarry of Renli No. 5 pegmatite. Samples HNRL-1 to HNRL-5 were used for physical analyses, and samples H-1 to H-7 were used for geochemical and spectroscopic analyses.

Physical properties of all the samples were determined with a refractometer (FGR-002A, Shenzhen Fable Jewellery Technology Co., Ltd., Shenzhen, China), long-wave (365 nm) and short-wave (254 nm) UV lamps (FUV-4, Shenzhen Fable Jewellery Technology Co., Ltd., Shenzhen, China), and an apparatus (Fable, Shenzhen Fable Jewellery Technology Co., Ltd., Shenzhen, China) for hydrostatic specific gravity testing. Internal features were observed under a binocular gemological microscope and a polarizing microscope (FGM-R1S-15, Shenzhen Fable Jewellery Technology Co., Ltd., Shenzhen, China).

Major element compositions of minerals were acquired at the Beijing ZKKY GeoAnalysis Laboratory Co., Ltd. (Beijing, China), using a JXA-8230 Electron Microprobe Analyzer (EMPA). The operating conditions include 15 kV acceleration voltage, 20 nA beam current, and 5 μm spot size. The background and peak position measurement time is set to 5 and 10 s, respectively. Quantitative analysis of minerals is calibrated using the following natural and synthetic standards: Quartz for Si, jadeite for Al and Na, albite for Na, wollastonite for Ca, apatite for P, phlogopite for K and F, forsterite for Mg, TiO_2 for Ti, $MnTiO_3$ for Mn, Fe_2O_3 for Fe, spinel for Cr, phlogopite for Cs, and NaCl for Cl. The detection limit of most elements is 40–200 ppm. Automatic ZAF correction was performed for all data. The analytical results were normalized based on 3 (Be + Li), where Li = (Na + K + Cs) − (Mg + Fe) (assuming that all Fe occurs as Fe^{2+}), and 18 O apfu [28].

Trace element analyses (incl. rare earth elements (REEs)) were performed on an Agilent 7900 inductively coupled plasma mass spectrometry (ICP-MS) (USA) at the Nanjing Hongchuang Exploration Technology Service Co., Ltd. (Nanjing, China). The samples were ground in an agate mortar to 200 mesh. The analysis procedure follows the Silicate Rocks-Part 30 according to the method recommended by the China State Standard (GB) [29]. The silicate rock samples were dissolved via closed pressure acid digestion: 50 mg of rock powder was weighed directly into a steel-jacketed high-pressure polytetra fluoroethylene bomb, and then dissolved in an acid mixture of 1.5 mL of 29 mol/L HF and 1 mL of 15 mol/L HNO_3 at 190 °C for 72 h. USGS reference materials of basalt (BCR-2, BHVO-2) and andesite (AVG-2) were analyzed for quality control. The analytical uncertainty of all trace elements for the reference materials is within ±10%. Data calibration and result monitoring were achieved by external standard and internal standard (Rh dopped). A total of 47 elements were measured (five times per element), with precision (1 RSD) better than 5%.

X-ray powder diffraction (XRD) analysis was performed on a BRUKER AXE D8 ADVANCE X-ray diffractometer (Germany) using the graphite monochromatized CuKα radiation at the School of Material Engineering, Jinling Institute of Technology (Nanjing, China). The tube voltage and current are 40 kV and 40 mA, respectively. The analysis used 5–70° range, continuous scanning mode, 6°/min scanning speed, 0.02° step size, and 0.2 s dwell time.

Infrared spectroscopy was recorded by a BRUKER TENSOR 27 Fourier-transform infrared spectrometer (FTIR) at the Gemstone Research Laboratory, School of Gemology, China University of Geosciences (Beijing, China), in transmission mode with 100 scans and 4 cm^{-1} resolution. Sample pellets were prepared by grinding ~1 mg of the sample with 100 mg KBr. The scanning range is 4000–400 cm^{-1}.

Raman spectroscopy was acquired at the same laboratory, using an HOR-IBAHR evolution laser Raman spectrometer. The analysis used 400–4000 cm^{-1} scanning range, 532 nm laser wavelength, 30–40 mW power, and 1 cm^{-1} resolution.

4. Results

4.1. Physical Properties

Physical properties of the beryl samples are summarized in Table 1. The beryl crystals are clear to milky, light to medium blue, euhedral to subhedral, and up to 6.6 cm long (Table 1; Figure 4). Some crystals develop parallel twinning (Figure 4f), along with etch figures and striations (Figure 4c,g). Incomplete cleavages are observed perpendicular to the crystal c-axis (Figure 4h), which could affect the gemstone quality of these crystals. The samples have a refractive index of 1.575–1.585, birefringence of 0.005–0.007, and specific gravity of 2.65–2.70. Dichroism intensity varies with color intensity, and is usually medium-light blue and colorless. All the samples are typically inert to long- and short-wave UV radiation. The oriented rectangular two-phase fluid inclusions are common in the samples (Figure 4i). Standard physical analyses indicate that these samples resemble a natural aquamarine [30].

Table 1. Physical properties of beryl from the Renli No. 5 pegmatite.

Scheme	Size (cm)	Form	Color	Clarity	Refractive Index	Birefringence	Pleochroism	Specific Gravity	Fluorescence	Internal Features
HNRL-1	6.6 × 2.8 × 2.6	Hexagonal	Medium blue	Subtranslucent	1.578–1.585	0.007	_	2.70	Inert	Abundant fissures
HNRL-2	1.3 × 0.7 × 0.6	Short hexagonal	Light blue	Translucence	1.575–1.582	0.007	Light blue/colorless	2.67	Inert	Uneven color
HNRL-3	1.9 × 1.7 × 1.7	Irregular	Light blue	Subtranslucent	1.577–1.583	0.006	_	2.69	Inert	Abundant fissures
HNRL-4	1.9 × 1.5 × 1.3	Irregular	Blue	Translucence	1.579–1.585	0.006	Blue/colorless	2.65	Inert	Abundant fissures
HNRL-5	1.7 × 1.1 × 1.0	Short hexagonal prismatic	Light greenish blue	Translucence	1.580–1.585	0.005	Light blue/colorless	2.69	Inert	Incomplete cleavage; Parallel twinning with striations along the c-axis

Note: "_"—Unable to test.

4.2. Geochemical Analysis

The beryl chemical compositions are presented in Table 2. All the samples have narrow ranges of major element contents (wt%): SiO_2 (65.421–67.309), Al_2O_3 (17.804–18.200), BeO (13.095–13.826), and very low CaO (0.005–0.009), P_2O_5 (0–0.015), MnO (0–0.021), TiO_2 (0–0.020), Cr_2O_3 (0–0.027), MgO (0–0.094). The average contents (wt%) of SiO_2 (66.326) and BeO (13.604) are close to the theoretical values, and the content of Al_2O_3 (17.978) is slightly lower than the theoretical value [31]. An excess of Si atoms (6.019–6.045 apfu) often occurs in the unit formulae, and could be ascribed to high silica activity in the crystallization environment [9]. The H_2O content is 1.477 to 1.905 wt%, which is calculated using an empirical formula [32]. Total iron content (FeO^T) ranges up to 0.690 wt%. The contents of alkali metals (wt%) are 0.389 to 1.321, with 0.256 to 0.760 Na_2O, 0.005 to 0.009 Li_2O, 0.053 to 0.221 Cs_2O, and 0.010 to 0.033 K_2O (Table 2). The Na_2O content was higher than the other alkali metals in all samples. Major inclusions in the beryl samples are quartz, albite, microcline, and muscovite (Table 3).

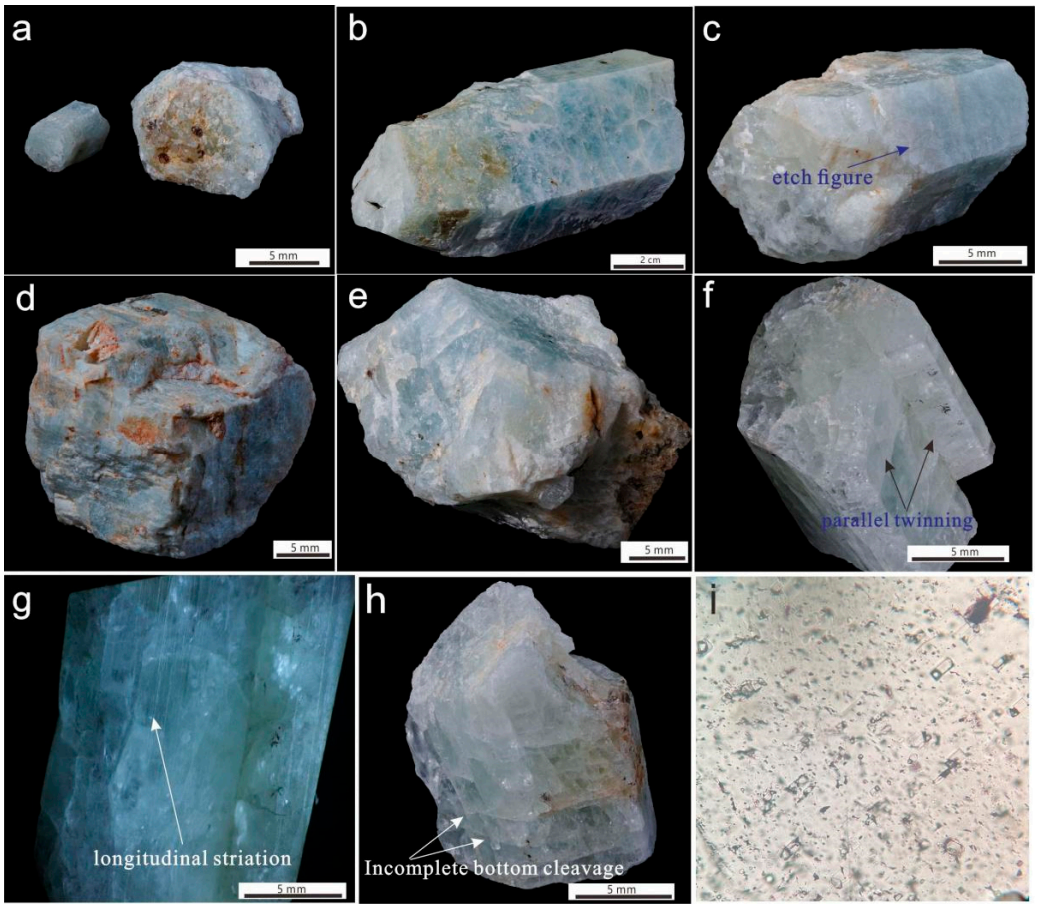

Figure 4. Representative hand-specimen photographs of beryl from the No. 5 pegmatite: (**a**) Hexagonal columnar beryl crystal; (**b**) columnar crystal (HNRL-1); (**c**) short columnar crystal with uneven color and etch figures on the surface (HNRL-2); (**d**) irregular crystal (HNRL-3); (**e**) irregular crystal (HNRL-4); (**f**) crystal with parallel twinning (HNRL-5); (**g**) crystal with longitudinal striation (HNRL-5); (**h**) crystal with incomplete bottom cleavage (HNRL-5); (**i**) lineated rectangular two-phase fluid inclusions (plan polar; 60×).

Table 2. Representative EMPA results of beryl from the No. 5 pegmatite (wt%).

Samples	H-1	H-2	H-3	H-4	H-5	H-6	H-7	Avg.
SiO_2	67.309	66.823	66.234	66.746	65.421	65.595	66.154	66.326
Al_2O_3	18.200	17.912	17.917	17.804	18.040	17.930	18.040	17.978
BeO*	13.826	13.614	13.347	13.447	13.187	13.095	13.275	13.399
Li_2O*	0.058	0.120	0.235	0.204	0.230	0.307	0.267	0.203
CaO	0.006	0.007	0.006	0.009	0.005	0.009	0.009	0.007
P_2O_5	0.006	0.002	0.003	0.001	0.015	0.006	0.000	0.005
Cs_2O	0.065	0.078	0.145	0.053	0.151	0.221	0.153	0.124
FeO^T	0.358	0.477	0.690	0.501	0.222	0.445	0.485	0.454
MnO	0.003	0.018	0.017	0.021	0.000	0.006	0.004	0.010
Cr_2O_3	0.014	0.021	0.027	0.000	0.000	0.027	0.017	0.015
TiO_2	0.000	0.004	0.000	0.004	0.000	0.020	0.011	0.006
Na_2O	0.256	0.427	0.738	0.621	0.525	0.760	0.714	0.577
MgO	0.018	0.084	0.000	0.020	0.014	0.094	0.054	0.041
F	0.022	0.053	0.000	0.049	0.000	0.006	0.000	0.019
K_2O	0.010	0.027	0.033	0.024	0.021	0.033	0.025	0.025
Cl	0.002	0.002	0.033	0.002	0.013	0.010	0.005	0.010

Table 2. *Cont.*

Samples	H-1	H-2	H-3	H-4	H-5	H-6	H-7	Avg.
H_2O*	1.477	1.623	1.887	1.787	1.706	1.905	1.866	1.750
Total	101.289	101.091	101.352	101.452	99.713	100.57	101.172	100.948
$Na_2O + K_2O + Cs_2O + Li_2O$	0.389	0.652	1.151	0.902	0.927	1.321	1.159	0.929
Si^{4+}	6.059	6.049	6.013	6.029	6.003	6.001	6.007	6.023
Al^{3+}	1.931	1.911	1.917	1.895	1.951	1.933	1.930	1.924
Be^{2+}	2.979	2.956	2.914	2.926	2.915	2.887	2.902	2.926
Li^{+}	0.021	0.044	0.086	0.074	0.085	0.113	0.098	0.074
Fe^{2+}	0.027	0.036	0.052	0.038	0.017	0.034	0.037	0.034
Mg^{2+}	0.002	0.011	0.000	0.003	0.002	0.013	0.007	0.005
Mn^{2+}	0.000	0.001	0.001	0.003	0.000	0.000	0.000	0.001
Cr^{3+}	0.001	0.002	0.002	0.002	0.000	0.002	0.001	0.001
Ti^{4+}	0.000	0.000	0.000	0.000	0.000	0.001	0.001	0.000
Na^{+}	0.045	0.075	0.130	0.109	0.093	0.135	0.126	0.102
K^{+}	0.001	0.003	0.004	0.003	0.002	0.004	0.003	0.003
Cs^{+}	0.002	0.003	0.006	0.002	0.006	0.009	0.006	0.005

Note: Chemical compositions of each sample listed here are the average of at least five EMPA tests. Formula calculations of beryl were based on 18 O apfu. Li_2O* and BeO* were estimated by stoichiometry assuming Li = Na + K + Cs − (Fe + Mn) and Be = 3-Li [28]; FeO^T = total iron content; H_2O was estimated from H_2O wt% = (Na_2O in wt% + 1.4829)/1.1771 [32].

Table 3. Representative EMPA results of quartz, albite, microcline, and muscovite in the beryl samples (wt%).

Samples	H-5-1	H-6-1	H-7-1	H-5-2	H-6-2	H-6-3	H-7-2	H-5-3	H-7-3
SiO_2	99.33	99.1	98.89	67.65	68.19	65.11	64.64	44.99	46.09
Al_2O_3	0.04	0.01	0.03	20.09	20.26	18.43	18.39	35.64	33.14
CaO	0.00	0.00	0.01	0.56	0.71	0.00	0.00	0.01	0.00
P_2O_5	0.01	0.01	0.00	0.17	0.07	0.00	0.00	0.00	0.02
Cs_2O	0.03	0.00	0.00	0.00	0.00	0.00	0.05	0.01	0.00
FeO	0.01	0.02	0.00	0.02	0.03	0.00	0.00	3.52	3.95
MnO	0.00	0.00	0.00	0.00	0.00	0.00	0.00	0.06	0.11
Cr_2O_3	0.01	0.04	0.00	0.00	0.00	0.00	0.04	0.03	0.00
TiO_2	0.00	0.00	0.05	0.01	0.00	0.06	0.00	0.05	0.13
Na_2O	0.05	0.05	0.00	10.93	10.9	1.06	0.31	0.42	0.37
MgO	0.00	0.01	0.00	0.00	0.00	0.00	0.00	0.15	0.79
F	0.00	0.04	0.00	0.00	0.01	0.00	0.03	0.55	0.93
K_2O	0.01	0.03	0.01	0.09	0.13	14.88	15.88	10.41	10.27
Cl	0.00	0.01	0.00	0.01	0.01	0.01	0.00	0.00	0.01
Total	99.5	99.35	99.01	99.52	100.31	99.71	99.49	95.96	95.99
Minerals	quartz	quartz	quartz	albite	albite	microcline	microcline	muscovite	muscovite

The beryl samples have relatively high Li (1413–1435 ppm), Cs (759–1138 ppm), Zn (252–360 ppm), Rb (29–41 ppm), and Ga (15–17 ppm) concentrations, whilst the contents of other trace elements are below 10 ppm (Table A1). The total REE elements (∑REEs) are very low (0.32–0.7 μg/g), with relative enrichment of light REEs (LREE/HREE = 15–16.5) (Table A2).

4.3. XRD Results

The XRD analyses show that the peak shapes and positions of the beryl samples are basically the same, and the main d-values are around 4.5883 (002), 3.9767 (200), 3.2506 (112), 3.0109 (210), 2.8626 (211), 2.5199 (212), 2.1503 (311), 1.9925 (204), 1.7402 (304), 1.6276 (224), 1.5138 (413), 1.4324 (324) (Table 4; Figure 5). In addition, quartz inclusions with main d-values of 4.2451 (100) and 3.3367 (101) are common in all samples (Figure 5), which is consistent with the EMPA results (Table 3). The MDI Jade 6.0 software was used to calculate the unit-cell parameters of beryl. The results show that a_0 ranges from 0.9197 to 0.9210 Å and

c_0 ranges from 0.9167 to 0.9185 Å (Table 4). The unit-cell volume is 671.8 to 674.6 Å^3. Beryls can be divided into three groups based on the lattice parameters (c_0/a_0) [9]: (1) "Octahedral" beryls: c_0/a_0 = 0.991 to 0.996, with Al ⇌ Me^{2+} being the main isomorphous replacement (alkalis in structural channels to charge balance); (2) "tetrahedral" beryls: c_0/a_0 = 0.999 to 1.003, with Be ⇌ Li being the main substitution; (3) "normal" beryls: c_0/a_0 = 0.997 to 0.998, with the occurrence of both substitutions aforementioned. The samples have c_0/a_0 = 0.995 to 0.997 (Table 4), which pertains to the "octahedral" to "normal" beryl series. Therefore, there are both tetrahedral and octahedral substitutions in our beryl samples.

Table 4. The unit-cell parameters (Å), unit-cell volume of the beryl samples, and their substitution series assignment after [9].

Samples	a_0 (Å)	c_0 (Å)	V (Å^3)	c_0/a_0	Group
H-3	0.9211	0.9178	674.4	0.996	Octahedral
H-4	0.9195	0.9165	671.1	0.997	Normal
H-5	0.9196	0.9168	671.5	0.997	Normal
H-6	0.9190	0.9148	669.2	0.995	Octahedral
Avg.	0.9204	0.9177	673.3	0.997	

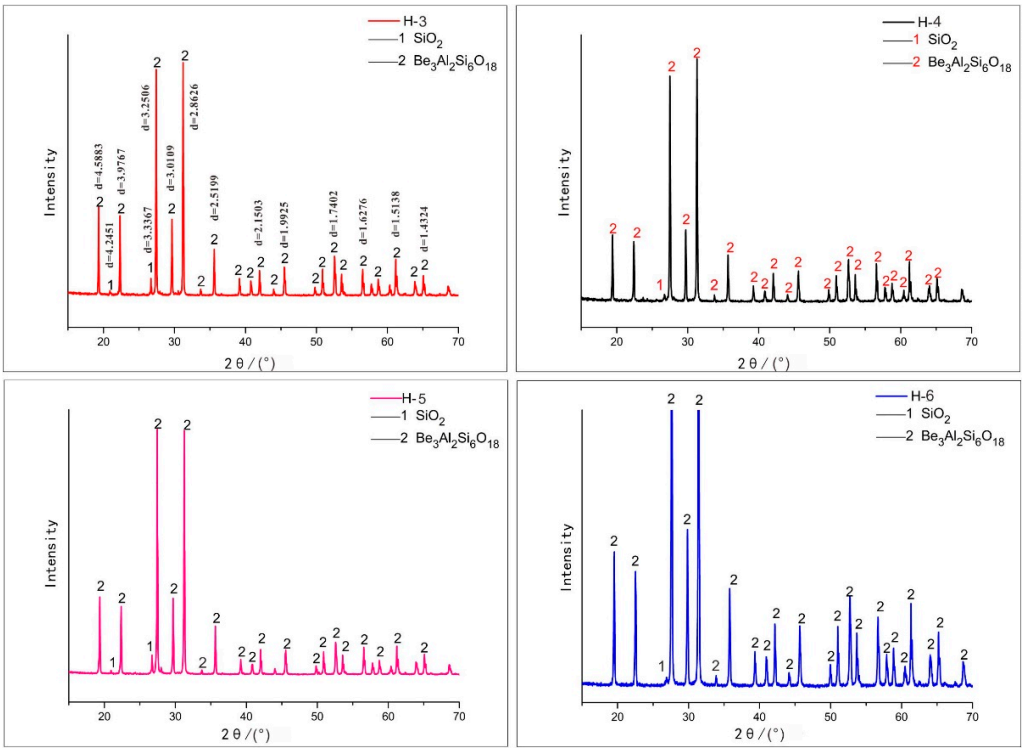

Figure 5. XRD results of beryl from the No. 5 pegmatite.

4.4. Infrared Absorption Spectroscopic Results

Absorption data in the 1400–400 cm^{-1} range are presented in Table 5 and illustrated in Figure 6. In this range, the beryl samples show clear, strong, and nearly identical absorption bands, caused by the vibration of the structural skeleton [Si_6O_{18}] group [33–35]. Compared with the standard infrared spectrum of beryl, the absorption bands of our samples generally shift toward higher wave numbers (up to 13 cm^{-1}; Table 5), which is associated with the substitution of elements, such as Fe, Cr, V, Li, Ti, and Mn into the crystal lattice. These substitutions would increase the length of M-O bond, weaken the bonding with oxygen, and strengthen the vibration, thus increasing the vibration frequency [35,36]. No (or very weak) peaks associated with CO_2 are observed in our samples (Table 5) [33].

Table 5. IR absorption peaks and corresponding band assignments of beryl from the No. 5 pegmatite.

H-1	H-2	H-3	H-4	H-5	Assigned Band [16,33–35,37]	Standard IR Spectra
493	490	493	495	493	ν(Si-O), ν(M-O), and their coupled vibrations	
526	529	528	525	528	ν(Si-O), ν(M-O), and their coupled vibrations	
595	595	595	594	595	ν(Si-O), ν(M-O), and their coupled vibrations	
650	652	647	649	649	ν(Be-O)	650
680	682	681	680	679	ν(Be-O)	680
745	745	749	744	742	ν(Be-O)	740
810	810	813	810	809	ν(Be-O)	800
957	958	956	n.d.	955	ν(Si-O)	950
1016	1017	1014	1018	1017	ν(Si-O)	1015
1074	n.d.	n.d.	1066	n.d.	ν(Si-O)	
1145	1146	1145	1146	1149	ν(Si-O)	
1200	1200	1200	1200	1200	ν(Si-O)	1195
1635	1633	1634	1634	1635	ν_2 H_2O type II	
2337	n.d.	n.d.	n.d.	2329	νCO_2	
2377	n.d.	n.d.	n.d.	2378	νCO_2	
3595	3595	3594	3595	3595	ν_1 H_2O type II	
3650	3646	n.d.	3651	3652	ν_1 H_2O type I	
n.d.	n.d.	3658	n.d.	n.d.	ν_3 H_2O type II	
3671	3671	n.d.	3670	3671	ν_3 H_2O type II	
3697	3698	3699	3699	3700	ν_3 H_2O type I	

Note: ν_1, symmetric stretching; ν_2, deformation; ν_3, asymmetric stretching; M, metal ion; n.d., not detected.

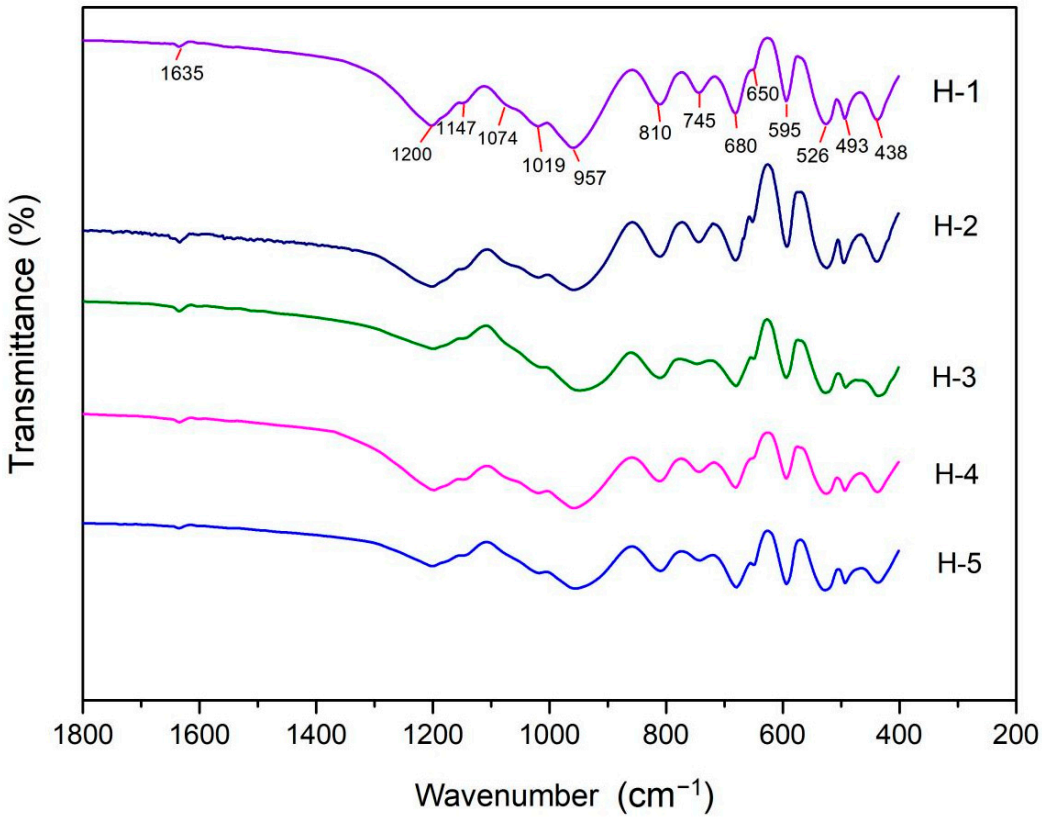

Figure 6. Infrared absorption spectra of beryl in the 1800–400 cm^{-1} range.

Details of the water-related absorption in the 4000–3000 cm^{-1} range are presented in Table 5 and illustrated in Figure 7. Two types of H_2O molecules are discerned in all beryl samples. Type-I H_2O (bands at ca. 3698 and 3595 cm^{-1}, stretching vibrations) is not connected with alkali [9,33]. Type-II H_2O (bands at ca. 3670, 3660, 3650 cm^{-1}, stretching vibrations) and ~1635 cm^{-1} (bending vibrations) is connected with alkalis [9,33].

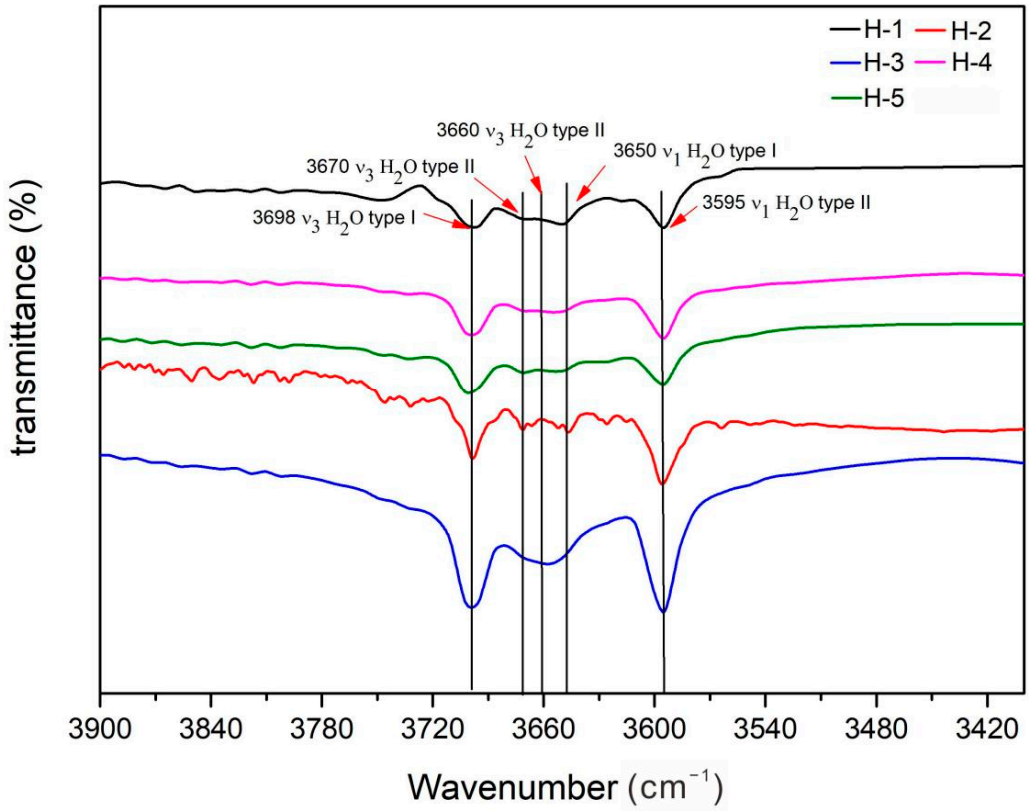

Figure 7. Infrared absorption spectra of beryl in the 3900–3400 cm^{-1} range.

4.5. Raman Spectroscopic Results

Adams and Gardner (1974) obtained all Raman shifts of beryl by the factor group analysis in single crystal spectra [38]. Since then, many authors have discussed the Raman spectral characteristics from various aspects [3,33,35,37,39], yet it remains controversial to assign modes to bands, especially for high frequencies where both Si-O vibrations and mixed Si-O and Be-O modes exist [35]. There are six normal vibration modes of beryl: $T_g = A_{1g} + A_{2g} + B_{1g} + B_{2g} + E_{1g} + E_{2g}$, among which A_{1g}, E_{1g}, and E_{2g} are Raman activities [40]. Spectra of all the beryl samples in the 200–4000 cm^{-1} range are practically identical (Figure 8; Table 6). The main Raman bands are around 320, 398, 687, 1004, and 1068 cm^{-1} (Figure 8a). The bands in the 200–1400 cm^{-1} range are structural vibrations, which connected with the stretching and bending vibrations of Si-O, Be-O, and Al-O [35]. The weak bands in the range 1236–1241 cm^{-1} belong to the CO_2 vibration [34,35]. Two types of H_2O molecules are also visible in the 3500–3700 cm^{-1} range (Figure 8b), both of which can be described as bands originated from symmetric stretching vibrations of the bond in water molecules [33]. Type-I H_2O is at 3607 cm^{-1}, whilst type-II H_2O is at 3598 cm^{-1} [33]. Type-I H_2O clearly dominated over type-II H_2O, confirming the fewer type-II water molecules and low alkali contents in the beryl samples [34]. All the bands at 3598 cm^{-1} are broader than those at 3607 cm^{-1}, possibly due to the combination of more than one band at 3598 cm^{-1} [35].

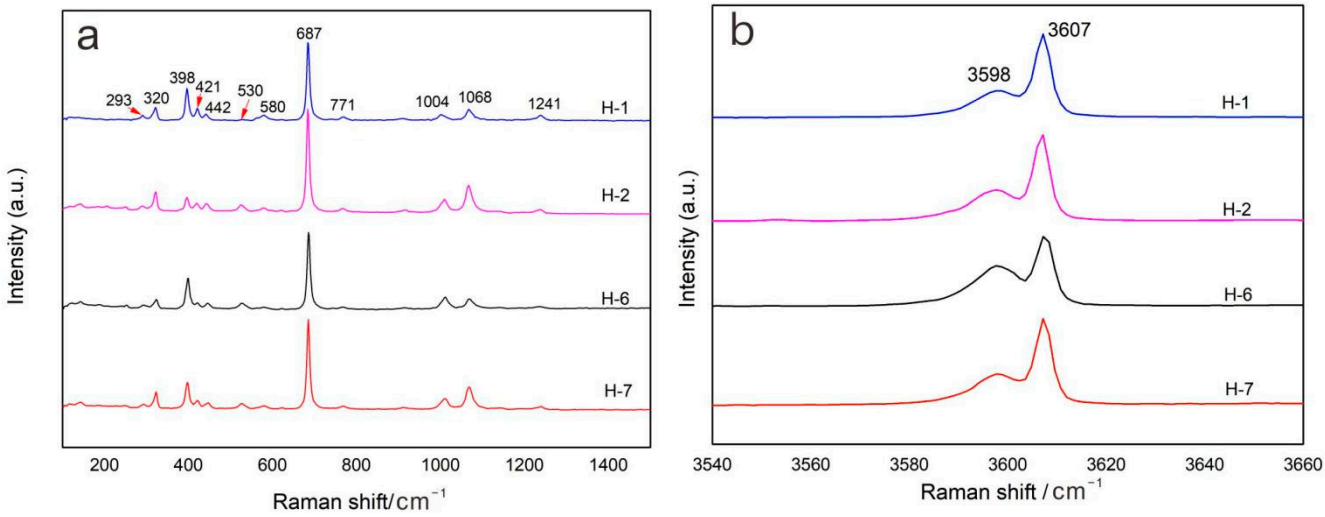

Figure 8. Raman spectra in the (**a**) 200–1400 cm^{-1} and (**b**) 3500–3700 cm^{-1} range.

Table 6. Raman peaks of beryl from the No. 5 pegmatite.

H-1	H-2	H-6	H-7	Band Assignments	Raman Shift in Refs. [3,33,35,37,38,40]
293	290	293	294	E_{1g} + E_{2g} overlap	289/291/297
320	320	323	323	A_{1g} + E_{2g} overlap	315/318/324/326
398	396	399	398	A_{1g} + E_{2g} overlap	281/383/394/395/400
421	419	420	423	E_{2g}	420/451/424
442	444	445	448	E_{1g} + E_{2g} overlap	442/443/444/449/450
530	526	527	528	ν(Al-O), E_{1g}	526/527/529
580	580	580	580	E_{2g}	581/580/583
619	620	n.d.	622	A_{1g}	621/626
687	684	686	687	ν(Be-O), A_{1g} + E_{2g}	683/686
771	766	768	770	ν(Al-O), E_{1g} + E_{2g} overlap	769/770/772
911	916	916	913	ν(Si-O), E_{1g} + E_{2g}	914/918
1004	1009	1010	1010	ν(Si-O), E_{1g} + E_{2g}	1001/1005
1068	1068	1069	1069	ν(Si-O), A_{1g}	1066/1068
n.d.	1139	1143	1144	ν(Si-O), A_{1g}	
1241	1236	1236	1240	ν_1 CO_2, E_{2g}	1225/1229/1243
3598	3598	3598	3598	ν_1 H_2O type II	3594/3597
3607	3607	3607	3607	ν_1 H_2O type I	3606–3609

Abbreviations: n.d., not detected.

5. Discussion

5.1. Classification and Crystal-Chemical Features of the Beryl

The No. 5 pegmatite beryl is overall characterized by a simple chemistry (Table 2). Beus [41] classified beryl into four types: (1) Alkali-free beryl (total R_2O < 0.5%, where R = Na, Li, Cs, K); (2) Na beryl (total R_2O > 0.5%, Na_2O = 0.5%–2%, Li_2O = 0.1%–0.5%); (3) Na-Li beryl (Li_2O = 0.5–1.5 and Na_2O = 1%–2.5%) and (4) Li-Cs beryl (Li_2O = 0.1%–1%, Cs_2O < 3%, Na_2O = 0.3%–1%). The average contents of R_2O and Na_2O of our samples are 0.93% and 0.58%, respectively. Therefore, the beryls from the No. 5 pegmatite belong to the Na-beryl type. Pauly et al. compiled the chemical data of beryl from important pegmatite districts worldwide [42]. By comparing the beryl trace element signatures in pegmatites worldwide, different geochemical groups can be distinguished according to the Fe-Mg-alkali and Li-Cs contents [42]. Figure 9 shows that the beryls from the No. 5 pegmatite belong to the low Li-Cs and low Fe-Mg-medium alkali (esp. Na) beryl groups.

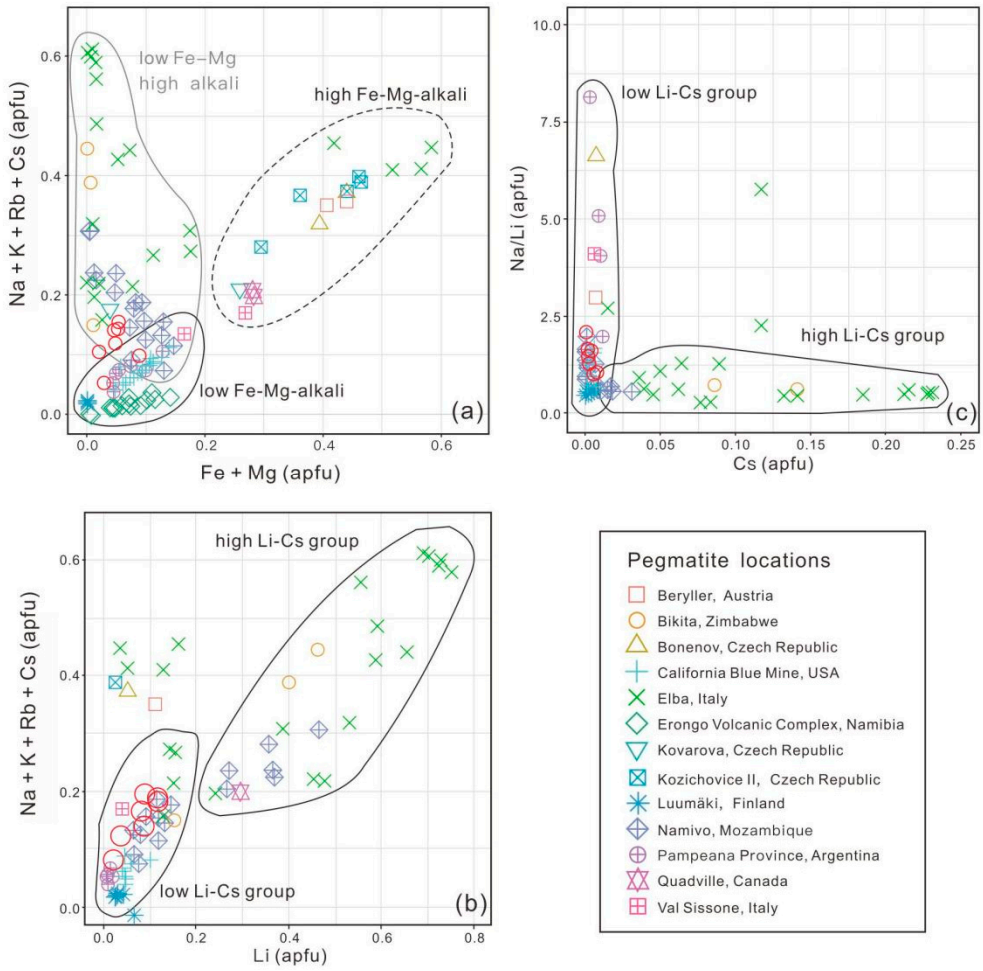

Figure 9. The classification of beryl. (**a**) Na + K + Rb + Cs vs. Fe + Mg; (**b**) Na/Li vs. Cs; (**c**) Na + K + Rb + Cs vs. Li (modified after [42]).

XRD results showed that most beryl samples belong to the "normal" beryl series. Therefore, isomorphic substitutions often occur in tetrahedral Be^{2+} and octahedral Al^{3+} sites. The primary occupant of the octahedral site (Al^{3+}) contains a maximum of 2 atoms, showing a relatively wide variation (1.900 to 1.957 apfu). A plot of the sum of substituting octahedral cations (Mg^{2+}, Fe^{2+}, Fe^{3+}, Mn^{2+}, Cr^{3+}, Ti^{4+}) vs. total Al shows a negative correlation (Figure 10a). The Si^{4+} analyses show a maximum of 6.045 apfu in the tetrahedral site, which permits only 6 atoms (Table 2). If the excess Si fits into the Al-bearing octahedral site as another substituting cation, the Al site is filled along the 1:1 substitution line and the data would show less variance (Figure 10b). Here, we assume that the octahedral substitution cations include Mg^{2+}, Fe^{2+}, Fe^{3+}, Mn^{2+}, Cr^{3+}, Ti^{4+}, and excess Si. Figure 10c shows the monovalent cations (in the channel) versus divalent cations plus Li. The diagonal line represents the charge balance between the substitution cations and the univalent cation (in the channel). The good agreement with the expected trend indicates that the Li mainly substitutes in the beryl crystal lattice. Combining the ionic radius of Li, we considered that Be^{2+} is substituted by Li^{+} and the alkali in channel (esp. Na) is a charge compensator (Figure 10d). Therefore, the substitution mechanisms of beryls from the No. 5 pegmatite can be expressed as follows:

$$^{O}Al^{3+} + {}^{C}\square \rightarrow {}^{O}R^{2+} + {}^{C}R \quad (1)$$

$$^{O}Al^{3+} \rightarrow {}^{O}R^{3+} \quad (2)$$

$$^{T1}Si^{4+} + {}^{C}\square \rightarrow {}^{T1}Al^{3+} + {}^{C}R^{+} \quad (3)$$

$$^{T2}Be^{2+} + ^{C}\square \rightarrow ^{T2}Li^{+} + ^{C}R^{+} \quad (4)$$

where R^{2+} and R^{3+} denote the divalent and trivalent cations, respectively; R^{+} denotes the alkali ions (Na^{+}, K^{+}, and Cs^{+}); O and T1 denote the Al in the octahedral site and Si in the tetrahedral site, respectively; T2 denotes the Be in the tetrahedral site; and □ denotes the channel site.

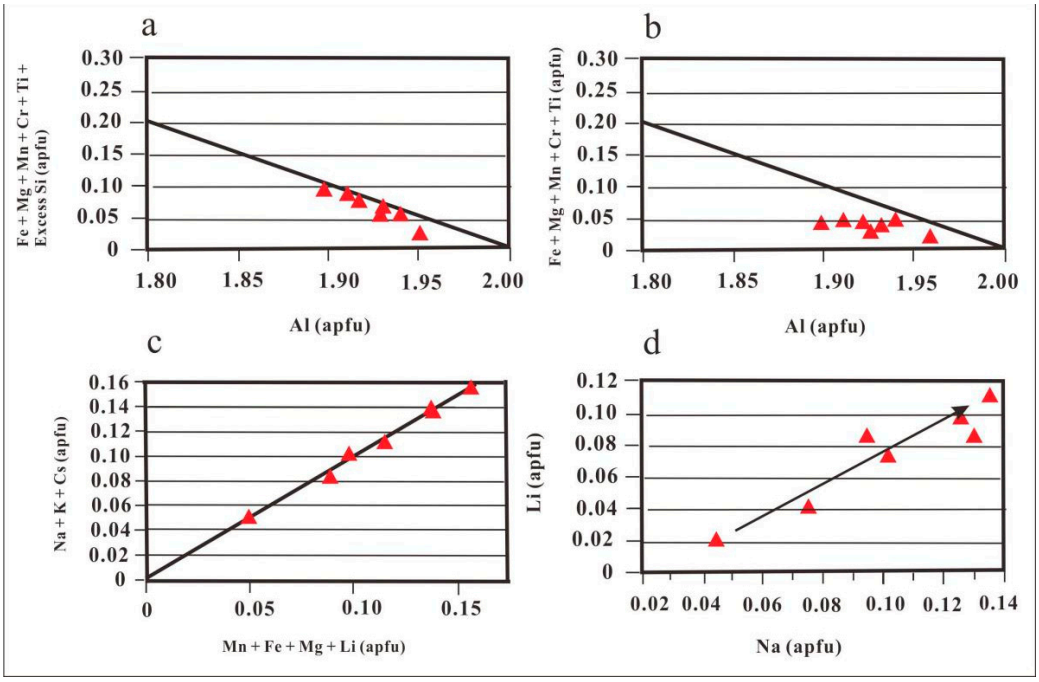

Figure 10. Binary plots that show major-element variations (apfu): (**a**) Al vs. total cations (incl. excess Si), which would substitute into the octahedral site; (**b**) Al vs. total cations (excl. excess Si), which would substitute into the octahedral site; (**c**) monovalent cations (in channel) vs. divalent cations plus Li; (**d**) Na vs. Li.

5.2. Occurrence of Cations in Structural Channel of the Beryl

Beryls have a hexagonal crystal structure with space group P6/mcc. This hexagonal ring structure was first determined by Bragg [43] and then refined by later studies [44–47]. Infrared and Raman spectroscopy can be useful to determine the structure of beryl [33–40]. Both the IR and Raman spectra in this study indicate the presence of CO_2 and two types of H_2O molecules (Tables 5 and 6). Based on previous studies [33–40] and spectral analysis of the beryl from the No. 5 pegmatite, we determined the positions of cations and molecules in the beryl channel, and revised the schematic model of the channels (Figure 11). Fukuda and Shinoda revealed two different positions in the beryl channel, i.e., 2a (0,0,1/4) between the rings and 2b (0,0,0) within the rings [48]. For the positions of cations and molecules in the channels, it is generally considered that the larger cations (incl. Cs^{+}, K^{+}, and occasionally Fe^{2+} and Fe^{3+}) occupy the 2a site, whereas the small cations (incl. Li^{+} and Na^{+}) occupy the smaller 2b site [33,48,49]. Due to the size limitation, water and CO_2 molecules should fit in the 2a site [14,16,34]. CO_2 molecules align with the molecular elongation perpendicular to the beryl sixfold c-axis [16]. Na^{+} is likely the dominant cation coordinated to type-II H_2O in our samples, as determined by chemical analyses (Table 2). Type-II H_2O coordinated with Na can exhibit two forms of coordination, i.e., doubly-coordinated type-II H_2O (IId) and singly-coordinated type-II H_2O (IIs) (Figure 12) [16,48,50]. The IR absorption bands of our samples at around 3595 and 1634 cm^{-1} were assigned to the ν_1 and ν_2 modes of type-II H_2O, which is caused by the single coordination between type-II H_2O molecule and a Na^{+} cation [48].

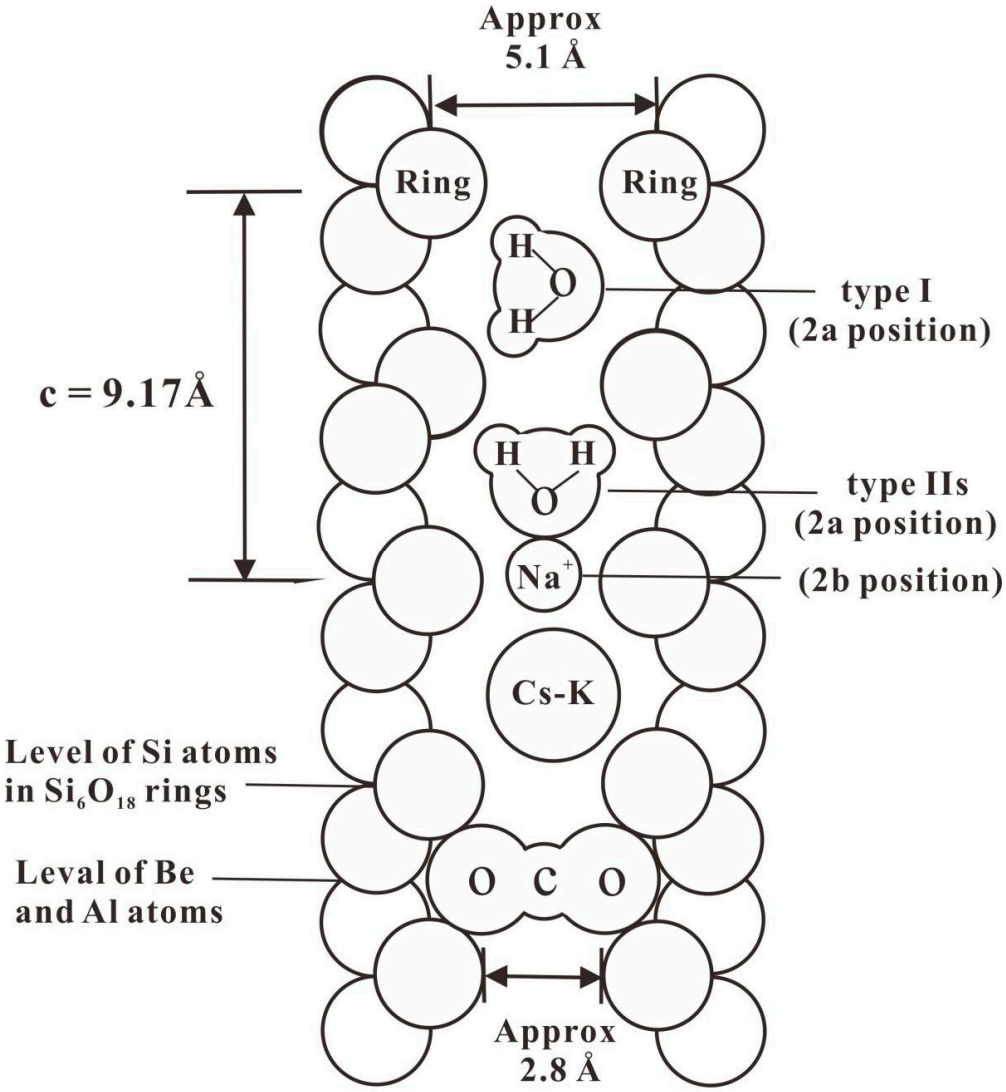

Figure 11. Schematic diagram of the beryl channels from the No. 5 pegmatite, showing structural oxygen atoms surrounding possible channel constituents (modified after [48]). The c-value is derived from the XRD analysis.

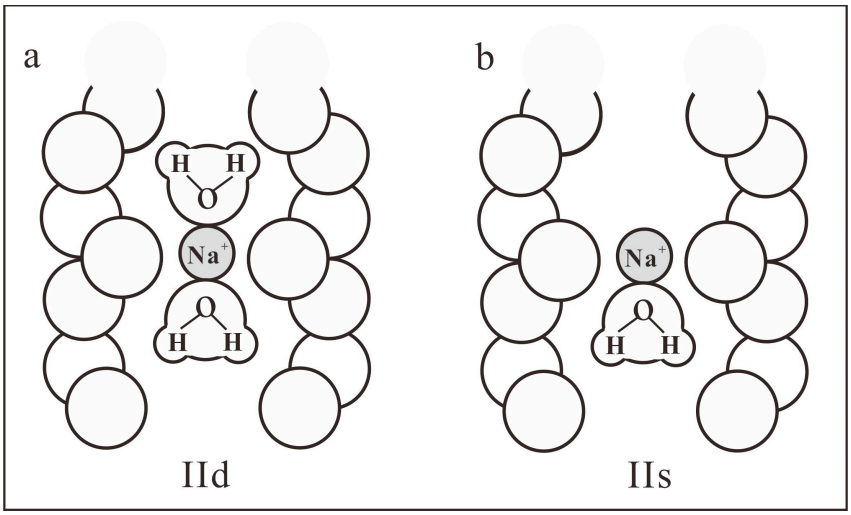

Figure 12. Possible coordination states of type-II H2O in the beryl channel: (**a**) Doubly coordinated and; (**b**) singly coordinated type-II H_2O (modified after [48]).

5.3. Preliminary Metallogenic Model for the Beryl in the No. 5 Pegmatite

Although Be is mainly enriched in the upper continental crust, its abundance is still very low (~2 ppm). Granite (esp. granitic pegmatite) and black shale are the main host rocks of Be, and it can occur in over a hundred minerals in nature, including beryl (dominant), micas, and albite [51]. Partial melting of protoliths that contain these Be-bearing minerals can promote Be enrichment [52]. Due to the low Be content in the Earth, the generation of beryl requires significant Be enrichment by magmatic differentiation and/or hydrothermal processes [53]. Hydrothermal beryl is distinguished by the high content of total alkalis (~14 wt%), and igneous beryl has total alkali contents of up to 7 wt%. The low alkali content (Table 2) indicates that the beryl from No. 5 pegmatite has an igneous origin.

The degree of magmatic differentiation of granites and pegmatites is closely related to rare metals mineralization [53,54]. The Na/Li, Na/Cs, and Mg/Fe values of beryl can determine the geochemical signature of the pegmatite host [5,55,56]. With increasing magma differentiation, the primary beryl would have higher Cs content, but lower Mg content and Na/Cs, Mg/Fe, and Na/Li values [18,55]. Evolution of pegmatitic melts can be inferred from the beryl Na/Li vs. Cs relationship. Trueman and Cerny [57] show a progressive evolution trend in pegmatite based on the variation of Na/Li (apfu) and Cs content (wt%) in beryl. Figure 13 shows the studied beryl samples plot in field A of the magmatic trend, and we suggested that our beryl samples belong to the primitive beryl type, and that the host pegmatite was from a less evolved magmatic source.

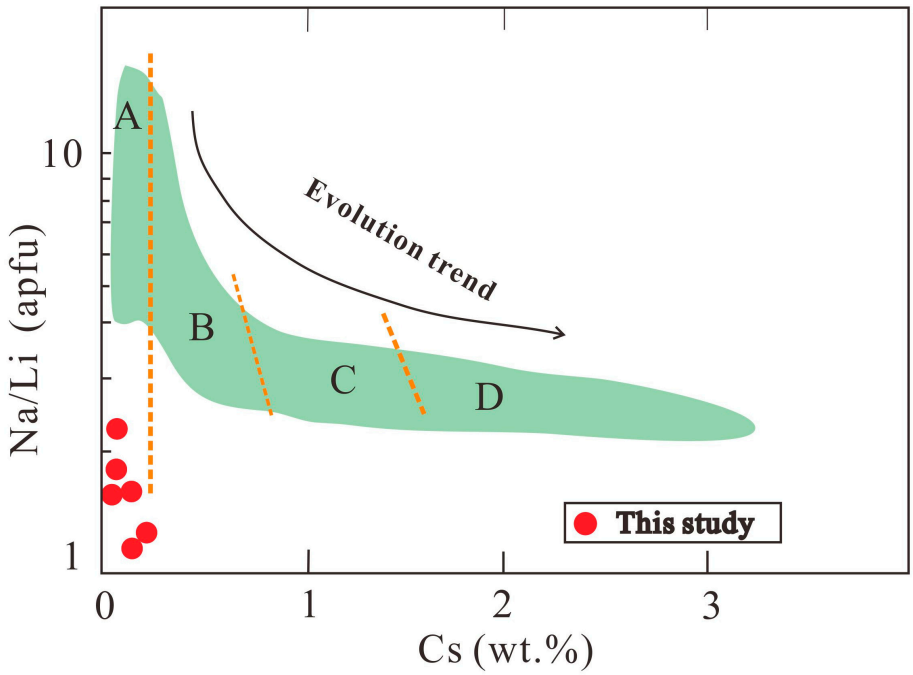

Figure 13. Diagram of Na/Li vs. Cs to compare the geochemical compositions of beryl from the No. 5 pegmatite with the magmatic trend proposed by Trueman and Cerny [57] and pegmatite type classification: (A) Barren and primitive beryl type and less-evolved pegmatite; (B) evolved beryl-columbite and beryl-columbite-phosphate pegmatite; (C) albite-spodumene and complex pegmatite; (D) highly-fractionated Li, Cs, and Ta-rich complex pegmatite. The orange dotted lines divide the different magmatic evolution zones.

The rare-metal pegmatites from Renli deposit show regular zoning of pegmatite types and rare-metal mineralization assemblages from the northeast to southwest [24] (Figures 1 and 3). Four zones can be recognized outward from the Mufushan batholith: Microcline pegmatite zone (P1); microcline-albite pegmatite zone (P2); albite pegmatite zone (P3); and albite-spodumene pegmatite zone (P4) (Figures 1 and 3). Field geological characteristics, as well as the previous chronological and isotopic studies indicate that these rare-metal peg-

matites have a close petrogenetic link with the Mufushan granite complex [20–27]. Field observation shows that the No. 5 pegmatite is layered and developed in the interlayer structures of the Lengjiaxi Group. Lepidolite Ar-Ar age on the No. 5 pegmatite yielded 125 ± 1.4 Ma (Early Cretaceous), representing the age of rare metal mineralization [22]. This age is significantly younger than the outcropping two-mica granite (zircon U-Pb age: 821.8–138.0 Ma) [20,58]. We proposed that the No. 5 pegmatite vein was formed during the multistage Mufushan granitic intrusions. The outcropping two-mica granite has an earlier emplacement than the mineralization, and is thus unlikely to be the parent rock of No. 5 pegmatite.

The beryl formation in the No. 5 pegmatite can be summarized as follows: The parent rock of No. 5 pegmatite vein was originated from the early to middle stage of the Yanshanian Mufushan granitic plutonism [24]. Deep magma may have ascended along structures in the Lengjiaxi Group schist to the shallow crustal level of the surface. The largely unfractured schist above the No. 5 pegmatite may have created a relatively enclosed space, which is conducive to the differentiation of granite-pegmatite melt. With increasing magma fractionation, the volatile (H_2O, F, C, CO_2)- and Be-rich melt may have formed Be compounds including $K_2(BeF_4)$, $Na(BeF_4)$, and $K_2(BeCO_3)$ [59]. When Be is enriched to a certain level, beryl (aquamarine) is formed at the early stage of pegmatite magma evolution.

5.4. Gemological Significance

Aquamarine is one of the most popular gem materials for centuries, prized for its beauty and rarity [60]. Beryl is widely distributed in granitic pegmatite, but high-quality aquamarines are uncommon. In recent years, a significant amount of gem-quality aquamarine has been recovered from the No. 5 pegmatite, and more production is expected in the future [22,26].

Field observation found that columnar beryl crystals from the No. 5 pegmatite with simple morphology occur commonly in zone II-V, in close association with microcline, albite, muscovite, and quartz (Figures 3 and 4), with sizes reaching several centimeters. Concentration of blue chromophore Fe is the highest among all transition metals (FeO^T = 0.222–0.690 wt%) (Table 2). Therefore, the beryl crystals with blue color can be classified as aquamarine, consistent with the physical analysis results (Table 1). In general, beryl from No. 5 pegmatite (some reaching gem-grade) are mostly light in color and have poor transparency.

Although the No. 5 pegmatite vein is rich in rare metals and gemstone resources, it has not been fully exploited, especially for the deep pegmatites at depth-level, which are better mineralized than their shallow-level counterparts [25]. The physical properties, geochemical, and spectral characteristics of beryl presented in this paper provide a reference for quality evaluation and identification of aquamarine in the district.

6. Conclusions

We conducted the first systematic chemical and spectroscopic analyses on beryl (aquamarine) from the Renli No. 5 pegmatite, and the major findings are summarized as follows:

(1) The No. 5 pegmatite vein contains abundant beryl mineralization. The beryl crystals are clear to milky, light to medium blue, commonly euhedral to subhedral, and up to 6.6 cm long. They are associated with garnet, morganite, lepidolite, and elbaite. The blue beryl with chromophore Fe can be classified as aquamarine, which has high economic value.

(2) By comparing the contents of Fe-Mg-alkali and Li-Cs of beryl in pegmatites worldwide, we concluded that the beryls from No. 5 pegmatite belong to the low Li-Cs and low Fe-Mg-medium alkali (esp. Na) beryl groups.

(3) Cation replacement in beryl is relatively simple. The substituting cations of beryl in the octahedral Al site include mainly Mg^{2+}, Fe^{2+}, Fe^{3+}, Mn^{2+}, Cr^{3+}, Ti^{4+}, and excess Si. The tetrahedral Be site is mainly replaced by Li. Alkalis in channel (esp. Na) are a charge compensator.

(4) Both of the obtained IR and Raman spectra indicate the presence of CO_2 and two types of H_2O molecules. The channel cation occupation of beryl from the No. 5 pegmatite occurs as follows: The larger cations (incl. Cs^+, K^+, H_2O, CO_2 and minor Fe^{2+} and Fe^{3+}) occupy the 2a site, whilst the smaller cations (incl. Li^+ and Na^+) occupy the smaller 2b site. Type-II H_2O molecules are singly-coordinated to a Na^+ cation.
(5) Concentration of Cs and Na/Li value in the beryl grains reflect a magmatic signature and suggest a relation to less-evolved granite.

Author Contributions: Conceptualization, Y.J. and J.L.; methodology, Y.J. and P.L.; validation, Y.J. and P.L.; formal analysis, Y.J.; investigation, Y.J.; resources, L.Z. and P.L.; writing—original draft preparation, Y.J.; writing—review and editing, Y.J. and J.L.; supervision, J.L. and Y.C.; project administration, P.L. and J.L.; funding acquisition, Y.J. and J.L. All authors have read and agreed to the published version of the manuscript.

Funding: This study was funded by the Jinling Institute of Technology High-level Talent Research Project (grant number jit-b-202127), the National Key R&D Program of China (2019YFC0605200), National Natural Science Foundation of China (42002109), the Geological Survey Project grants from the China Geological Survey (DD20221684).

Data Availability Statement: Not applicable.

Acknowledgments: We appreciate 311 Brigade of Hunan Nuclear Geology for their kind field support.

Conflicts of Interest: The authors declare no conflict of interest.

Appendix A

Table A1. Representative trace element compositions of beryl samples from No. 5 pegmatite (in ppm).

Samples	Li	B	V	Cr	Mn	Co	Ni	Cu	Zn	Ga	Ge
H-1	1434.57	8.56	2.38	4.78	28.72	0.19	0.19	1.91	360.14	16.58	0.90
H-2	1412.59	5.74	0.98	4.80	21.59	0.16	0.29	6.79	251.92	15.38	0.87
Samples	**Rb**	**Sr**	**Y**	**Zr**	**Nb**	**Mo**	**Cd**	**In**	**Sn**	**Sb**	**Te**
H-1	41.33	1.24	0.06	0.60	0.58	0.07	0.01	0.00	0.78	0.03	0.00
H-2	29.01	0.36	0.05	2.10	0.37	0.06	0.04	0.01	0.69	0.02	0.00
Samples	**Cs**	**Ba**	**Hf**	**Ta**	**W**	**Tl**	**Pb**	**Bi**	**Th**	**U**	
H-1	758.90	1.45	0.03	0.59	0.41	0.26	0.52	0.22	0.07	0.06	
H-2	1137.71	0.42	0.16	0.47	0.07	0.31	0.37	2.63	0.01	0.17	

Table A2. Representative REE compositions of beryl samples from No. 5 pegmatite (in ppm).

Samples	H-1	H-2
La	0.26	0.12
Ce	0.18	0.09
Pr	0.05	0.02
Nd	0.15	0.06
Sm	0.02	0.01
Eu	0	0
Gd	0.01	0.01
Tb	0	0
Dy	0.01	0.01
Ho	0	0
Er	0.01	0
Tm	0	0

Table A2. *Cont.*

Samples	H-1	H-2
Yb	0.01	0
Lu	0	0
TREE	0.7	0.32
LREE	0.66	0.3
HREE	0.04	0.02
LREE/HREE	16.5	15

References

1. Schulz, K.J.; DeYoung, J.H., Jr.; Seal, R.R., II; Bradley, D.C. Critical Mineral Resources of the United States-Economic and Environmental Geology and Prospects for Future Supply. In *Geological Survey Professional Paper*; U.S. Geological Survey: Reston, VA, USA, 2017; Volume 1802, pp. E1–E32.
2. Simmons, W.B.; Pezzotta, F.; Shigley, J.E.; Beurlen, H. Granitic pegmatites as sources of colored gemstones. *Elements* **2012**, *8*, 281–287. [CrossRef]
3. Charoy, B.; Noronha, F. Multistage growth of a rare-element, volatile-rich microgranite at Argemela (Portugal). *J. Petrol.* **1996**, *37*, 73–94. [CrossRef]
4. Černý, P. Mineralogy of beryllium in granitic pegmatites. *Rev. Miner. Geochem.* **2002**, *50*, 405–444. [CrossRef]
5. Wang, R.; Che, X.; Zhang, W.; Zhang, A.; Zhang, H. Geochemical evolution and late re-equilibration of Na-Cs rich beryl from the Koktokay #3 pegmatite (Altai, NW China). *Eur. J. Miner.* **2009**, *21*, 795–809. [CrossRef]
6. Grundmann, G.; Morteani, G. Multi-stage emerald formation during Pan-African regional metamorphism: The Zabara, Sikait, Umm Kabo deposits, South Eastern desert of Egypt. *J. Afr. Earth Sci.* **2008**, *50*, 168–187. [CrossRef]
7. Hawthorne, F.C.; Cooper, M.A.; Simmons, W.B.; Falster, A.U.; Laurs, B.M.; Armbruster, T.; Rossman, G.R.; Peretti, A.; Günter, D.; Grobety, B. Pezzottaite, $Cs(Be_2Li)Al_2Si_6O_{18}$: A spectacular new mineral related to the Beryl group, from Madagascar. *Mineral. Rec.* **2005**, *35*, 369–378.
8. Groat, L.A.; Rossman, G.R.; Dyar, M.D.; Turner, D.J.; Piccoli, P.M.B.; Schultz, A.J.; Ottolini, L. Crystal chemistry of dark blue aquamarine from the True Blue showing, Yukon Territory, Canada. *Can. Mineral.* **2010**, *48*, 597–613. [CrossRef]
9. Aurisicchio, C.; Fioravanti, G.; Grubessi, O.; Zanazzi, P.F. Reappraisal of the crystal chemistry of beryl. *Am. Mineral.* **1988**, *73*, 826–837.
10. Kim, C.C.; Bell, M.I.; McKeown, D.A. Vibrational analysis of beryl ($Be_3Al_2Si_6O_{18}$) and its constituent ring (Si_6O_{18}). *Phys. B Condens. Matter.* **1995**, *205*, 193–208. [CrossRef]
11. Aurisicchio, C.; Grubessi, O.; Zecchini, P. Infrared spectroscopy and crystal chemistry of the beryl group. *Can. Miner.* **1994**, *32*, 55–68. [CrossRef]
12. Groat, L.A.; Giuliani, G.; Marshall, D.D.; Turner, D. Emerald deposits and occurrences: A review. *Ore. Geol. Rev.* **2008**, *34*, 87–112. [CrossRef]
13. Aines, R.D.; Rossman, G.R. The high temperature behavior of water and carbon dioxide in cordierite and beryl. *Am. Miner.* **1984**, *69*, 319–327.
14. Wood, D.L.; Nassau, K. The characterization of beryl and emerald by visible and infrared absorption spectroscopy. *Am. Miner.* **1968**, *53*, 777–800.
15. Gatta, G.D.; Nestola, F.; Bromiley, G.D.; Mattauch, S. The real topological configuration of the extra-framework content in alkali-poor beryl: A multi-methodological study. *Am. Miner.* **2006**, *91*, 29–34. [CrossRef]
16. Fridrichová, J.; Bačík, P.; Bizovská, V.; Libowitzky, E.; Škoda, R.; Uher, P.; Ozdín, D.; Števko, M. Spectroscopic and bond-topological investigation of interstitial volatiles in beryl from Slovakia. *Phys. Chem. Min.* **2016**, *43*, 419–437. [CrossRef]
17. Viana, R.R.; Jordt-Evangelista, H.; Magela da Costa, G.; Stern, W.B. Characterization of beryl (aquamarine variety) from pegmatites of Minas Gerais, Brazil. *Phys. Chem. Min.* **2002**, *29*, 668–679. [CrossRef]
18. Uher, P.; Chudík, P.; Bačík, P.; Vaculovič, T.; Galiová, M. Beryl composition and evolution trends: An example from granitic pegmatites of the beryl-columbite subtype, Western Carpathians, Slovakia. *J. Geosci.* **2010**, *55*, 69–80. [CrossRef]
19. Merino, E.; Villaseca, C.; Orejana, D.; Jeffries, T. Gahnite, chrysoberyl and beryl co-occurrence as accessory minerals in a highly evolved peraluminous pluton: The Belvís de Monroy leucogranite (Cáceres, Spain). *Lithos* **2013**, *179*, 137–156. [CrossRef]
20. Li, P.; Li, J.K.; Pei, R.F.; Leng, S.L.; Zhang, X.; Zhou, F.C.; Li, S.M. Multistage Magmatic Evolution and Cretaceous Peak Metallogenic Epochs of Mufushan Composite Granite Mass: Constrains from Geochronological Evidence. *Earth Sci.* **2017**, *42*, 13. (In Chinese with English Abstract)
21. Yang, H.; Chen, Z.Y.; Li, J.K.; Xiong, X.; Wang, Z.; Zhou, F.C. Relationship between the mineralization and the evolution of mica and feldspar components of Renli-Chuanziyuan No. 5 Pegmatite, northeast Hunan. *Miner. Depos.* **2019**, *38*, 851–866. (In Chinese with English Abstract)
22. Li, P.; Liu, X.; Li, J.K.; Huang, Z.B.; Zhou, C.F.; Zhang, L.P. Petrographic and geochemical characteristics of Renli-Chuanziyuan No. 5 pegmatite, NE Hunan, and its metallogenic age. *Acta Geol. Sin.* **2019**, *93*, 1374–1391. (In Chinese with English Abstract)

23. Wang, Z.; Chen, Z.Y.; Li, J.K.; Li, P.; Xiong, X.; Yang, H.; Zhou, C.F. Indication of mica minerals for magmatic-hydrothermal evolution of Renli rare metal pegmatite deposit. *Miner. Depos.* **2019**, *38*, 1039–1052. (In Chinese with English abstract)
24. Li, P.; Li, J.K.; Chen, Z.Y.; Liu, X.; Huang, Z.B.; Zhou, F.C. Compositional evolution of the muscovite of Renli pegmatite-type rare-metal deposit, northeast Hunan, China: Implications for its petrogenesis and mineralization potential. *Ore. Geol. Rev.* **2021**, *138*, 0169–1368. [CrossRef]
25. Zhou, F.C.; Liu, X.; Li, J.K.; Huang, Z.B.; Xiao, G.Q.; Li, P.; Zhou, H.X.; Shi, W.K.; Tan, L.M.; Su, J.N.; et al. Metallogenic Characteristics and Prospecting Direction of Renli Super-Large Rare Metal Deposit in Hunan Province, China. *Geotecton. et Metallog.* **2019**, *43*, 77–91. (In Chinese with English Abstract)
26. Liu, X.; Zhou, F.C.; Huang, Z.B.; Li, J.K.; Zhou, H.X.; Xiao, G.Q.; Bao, Y.H.; Li, P.; Tan, L.M.; Shi, W.K.; et al. Discovery of Renli Superlarge Pegmatite-type Nb-Ta Polymetallic Deposit in Pingjiang, Hunan Province and its Significances. *Geotecton. et Metallog.* **2018**, *42*, 235–243. (In Chinese with English Abstract)
27. Zhou, F.C.; Li, P.; Liu, X.; Li, G.; Huang, Z.B.; Li, J.K.; Cheng, Y.S.; Su, J.N.; Zhang, L.P.; Chen, H.; et al. Petrographic and mineralogical characteristics of Renli rare metal deposit in Hunan Province and their geological implications: A case study of drill hole ZK708 of the No. 5 vein. *Miner. Depos.* **2021**, *40*, 753–775. (In Chinese with English Abstract)
28. Brand, A.A.; Groat, L.A.; Linnen, R.L.; Garland, M.I.; Breaks, F.W.; Giuliani, G. Emerald mineralization associated with the mavis lake pegmatite group, near Dryden, Ontario. *Can. Min.* **2009**, *2*, 315–336. [CrossRef]
29. *GB/T 14506.30-2010*; National Standards of the People' Republic of China: Methods for Chemical Analysis of Silicate Rocks-Part 30: Determination of 44 Elements. Standardization Administration of China Press: Beijing, China, 2010. (In Chinese)
30. Zhang, B.L. *Systematic Gemmology*; Geological Publishing House: Beijing, China, 2006.
31. Li, S.R.; Xu, H.; Shen, J.F. *Crystallography and Mineralogy*; Geological Publishing House: Beijing, China, 2008; pp. 220–221. (In Chinese)
32. Giuliani, G.; France-lanord, C.; Zimmermann, J.L.; Cheilletz, A.; Arboleda, C.; Charoy, B.; Coget, P.; Fontan, F.; Giard, D. Fluid composition, δD of channel H_2O, and $\delta^{18}O$ of lattice oxygen in beryls: Genetic implications for Brazilian, Colombian, and Afghanistani emerald deposits. *Int. Geol. Rev.* **1997**, *39*, 400–424. [CrossRef]
33. Łodziński, M.; Sitarz, M.; Stec, K.; Kozanecki, M.; Fojud, Z.; Jurga, S. ICP, IR, Raman, NMR investigations of beryls from pegmatites of the Sudety Mts. *J. Mol. Struct.* **2005**, *744–747*, 1005–1015. [CrossRef]
34. Wood, D.L.; Nassau, K. Infrared Spectra of Foreign Molecules in Beryl. *J. Chem. Phys.* **1967**, *47*, 2220–2228. [CrossRef]
35. Huong, L.T.T. Microscopic, Chemical and Spectroscopic Investigations on Emeralds of Various Origins. Ph.D. Thesis, Johannes Gutenberg University, Mainz, Germany, 2008.
36. Liang, T. The study of infrared absorption spectroscopic characteristics of emeralds. *J. Chan'an Univ.* **2003**, *25*, 10–13. (In Chinese with English Abstract)
37. Hofmeister, A.M.; Hoering, T.C.; Virgo, D. Vibrational spectroscopy of beryllium aluminosilicates: Heat capacity calculations from band assignments. *Phys. Chem. Min.* **1987**, *14*, 205–224. [CrossRef]
38. Adams, D.M.; Gardner, I.R. Single-crystal vibrational spectra of beryl and dioptase. *J. Chem. Soc. Dalton. Trans.* **1974**, *1*, 1502–1505. [CrossRef]
39. Griffith, W.P. Raman studies on rock-forming minerals. Part 1. Orthosilicates and cyclosilicates. *J. Chem. Soc. A Inorg. Phys. Theor.* **1969**, 1372–1377. [CrossRef]
40. Hagemann, H.; Lucken, A.; Bill, H.; Gysler-Sanz, J.; Stalder, H.A. Polarized Raman spectra of beryl and bazzite. *Phys. Chem. Min.* **1990**, *17*, 395–401. [CrossRef]
41. Beus, A.A. *Geochemistry of Berllium and Genetic Types of Beryllium Deposits*; Freemand and Co.: San Francisco, CA, USA, 1966.
42. Pauly, C.; Gysi, A.P.; Pfaff, K.; Merkel, I. Beryl as indicator of metasomatic processes in the California Blue Mine topaz-beryl pegmatite and associated miarolitic pockets. *Lithos* **2021**, *404*, 0024–4937. [CrossRef]
43. Bragg, W.L.; West, J. The structure of beryl, $Be_3Al_2Si_6O_{18}$. *Proc. Roy. Soc.* **1926**, *111*, 691–714.
44. Below, N.V.; Matveeva, R.G. The determination of the structural parameters of beryl by the method of bounded projections. *Dokl. Akad. Nauk. SSSR* **1951**, *6*, 69–82.
45. Gibbs, G.V.; Breck, D.W.; Meagher, E.P. Structural refinement of hydrous and anhydrous synthetic beryl, $Al_2(Be_3Si_6)O_{18}$ and emerald, $Al_{1.9}Cr_{0.1}(Be_3Si_6)O_{18}$. *Lithos* **1968**, *1*, 275–285. [CrossRef]
46. Morosin, B. Structure and thermal expansion of beryl. *Acta Cryst. B* **1972**, *28*, 1899–1903. [CrossRef]
47. Arivazhagan, V.; Schmitz, F.D.; Vullum, P.E.; Van-Helvoort, A.T.J.; Holst, B. Atomic resolution imaging of beryl: An investigation of the nano-channel occupation. *J. Microsc.* **2017**, *265*, 245–250. [CrossRef] [PubMed]
48. Fukuda, J.; Shinoda, K. Coordination of water molecules with Na+ cations in a beryl channel as determined by polarized IR spectroscopy. *Phys. Chem. Min.* **2008**, *35*, 347–357. [CrossRef]
49. Hawthorne, F.C.; Cerny, P. The alkali-metal positions in Cs-Li beryl. *Can. Miner.* **1977**, *15*, 414–421.
50. Zhukova, E.S.; Torgashev, V.I.; Gorshunov, B.P.; Lebedev, V.V.; Shakurov, G.S.; Kremer, R.K.; Pestrjakov, E.V.; Tomas, V.G.; Fursenko, D.A.; Prokhorov, A.S.; et al. Vibrational states of a water molecule in a nano-cavity of beryl crystal lattice. *J. Chem. Phys.* **2014**, *140*, 1089–7690. [CrossRef] [PubMed]
51. Sanders, I.S.; Doff, D.H. A blue sodic beryl from southeast Ireland. *Miner. Mag.* **1991**, *55*, 167–172. [CrossRef]
52. Rudnick, R.L.; Gao, S. 3.01-Composition of the continental crust. In *Treatise on Geochemistry*; Elsevier: Amsterdam, The Netherlands, 2003; Volume 3, pp. 1–64.

53. Wroński, M.; Wierzbanowski, K. Solubility and stability of beryl in granitic melts. *Am. Miner.* **1999**, *84*, 733–745. [CrossRef]
54. Aurisicchio, C.; Conte, A.M. Beryl from miarolitic pockets of granitic pegmatites, Elba, Italy: Characterization of crystal chemistry by means of EMP and SIMS analyses. *Can. Mineral.* **2012**, *50*, 1467–1488. [CrossRef]
55. Cerny, P. (Ed.) *Petrogenesis of Granitic Pegmatites*; Granitic Pegmatites in Science and Industry: Winnipeg, MB, Canada; Mineralogical Association of Canada: Quebec, QC, Canada, 1982; pp. 405–462.
56. Cerny, P.; Anderson, A.J.; Tomascak, P.B.; Chapman, R. Geochemical and morphological features of beryl from the Bikita granitic pegmatite, Zimbabwe. *Can. Mineral.* **2003**, *41*, 1003–1011. [CrossRef]
57. Trueman, D.L.; Cerny, P. Exploration for rare-element granitic pegmatites. In Proceedings of the Short Course in Granitic Pegmatites in Science and Industry, Winnipeg, MB, Canada, 13–16 May 1982; Mineralogical Association of Canada: Quebec, QC, Canada, 1982; pp. 463–493.
58. Huang, Z.B.; Li, P.; Zhou, F.C.; Liu, X.; Li, J.K.; Xiao, G.Q. Geochemical characteristics and genesis of the Neoproterozoic granites in Mufushan area. *J. Guilin. Univ. Technol.* **2018**, *38*, 614–624. (In Chinese with English Abstract)
59. Li, Z.L.; Mao, Y.H.; Lei, L.H.; Qiu, Z.L.; Niu, H.C. Physicochemical Conditions of the Formation of Beryl and Aquamarine in Mufushan Granopegmatite Deposit, Hunan Province, China. *Chin. J. Geophys.* **1994**, *13*, 326–339.
60. Prosperi, L.; Smith, C.P.; Gatta, G.D.; Pavese, A.; Adamo, I.; Diella, V.; Ajo, D. Aquamarine, Maxixe-type beryl, and hydrothermal synthetic blue beryl: Analysis and identification. *Gems Gemol.* **2009**, *44*, 214–226.